JOURNAL ARTICLE

A novel method to simultaneously estimate bacterial respiration and growth from oxygen dynamics

Ilgaz Cakin, Rebecca Millington, Samraat Pawar, Angus Buckling, Nicholas Smirnoff, Daniel Padfield, John Duffy, Gabriel Yvon-Durocher

ISME Communications, Volume 6, Issue 1, January 2026, ycag024,
https://doi.org/10.1093/ismeco/ycag024
Published: 05 February 2026 **Article history** ▾

Abstract

Bacterial growth and respiration are fundamental metabolic processes that drive energy transformation and allocation within organisms and impact carbon sequestration at the ecosystem scale. However, these traits are usually measured independently; bacterial growth is quantified with endpoint biomass measurements, while respiration is determined by monitoring oxygen or carbon dioxide. Because the two physiological traits are collected at different temporal and volumetric scales (hours-to-days for growth versus minutes-to-hours for respiration), reconciling them is challenging and often introduces scale-mismatch bias, obscuring causal links between metabolism and environmental drivers. In this study, we develop a novel method for quantifying the rates of bacterial growth and respiration from a single dissolved-oxygen time series. Our approach introduces a model that couples exponential biomass growth with biomass-specific respiration, enabling simultaneous inference of growth rate and respiration rate from each oxygen trajectory. We applied our high-throughput method to 15 bacterial taxa isolated from natural environments. Our approach yielded growth estimates in close agreement with measurements based on popular methods using optical density or flow cytometry ($R^2 > 0.9$) with no evidence of taxon-specific bias. We also tested our approach in quantifying the effects of temperature on respiration, growth, and carbon use-efficiency in *Pseudomonas* sp. Our method yielded typical unimodal thermal response curves for growth and respiration where rates were highest at

moderate temperatures, while carbon use efficiency increased with temperature, peaked around the growth thermal optimum (~30°C–35°C), and declined at the highest temperature. By quantifying respiration and growth within a single assay and in high throughput, our approach effectively enables measurement of microbial metabolic strategies and adaptations to stress. It offers a noninvasive and scalable tool for high-throughput phenotyping and studies of environmental perturbations, enabling a new class of trait-based microbial ecology that links cellular physiology to broader ecosystem function.

Issue Section: Original Article

Introduction

Microbial growth and respiration are essential physiological processes that drive the cycling of carbon and energy in ecosystems [1]. By decomposing organic matter and converting carbon into biomass, microbial communities play a key role in determining the distribution of carbon between biological pools and atmospheric CO_2 and, as such, in affecting biogeochemical fluxes at both local and global levels [2]. Bacteria comprise a significant fraction of total ecosystem biomass [2] and are a major component of total ecosystem respiration [3], emphasizing their critical contribution to ecosystem processes [4, 5]. At the cellular level, bacterial metabolic processes involve the allocation of energy between growth, leading to net biomass accumulation, and maintenance, which sustains necessary processes for cellular integrity [6, 7]. This balance varies across environmental conditions, physiological states, and stressors, shaping microbial carbon use and energetic efficiency [8, 9]. Empirical observations often describe total respiration as comprising (i) a maintenance component that is independent of the instantaneous growth rate but varies with factors such as temperature and (ii) a growth-associated component that is proportional to biomass synthesis [6, 9]. Understanding these components together is critical for linking cell metabolism to broader carbon fluxes at the ecosystem scale.

Despite this importance, growth and respiration are typically measured using distinct, asynchronous methods: oxygen uptake or CO_2 release for respiration and optical density, cell counts, or biomass yield for growth [10, 11]. When research questions aim to link growth and metabolism, e.g. by attempting to understand how environmental variation affects energy allocation, measuring growth and respiration across different scales can make reconciling these rate measurements challenging. For example, rates of growth measured via cell counts or biomass change over time are typically measured over timescales of several hours to days, while rates of respiration are measured over minutes to hours. Chemostats can circumvent some of these challenges by measuring growth and metabolic flux *in situ* at steady state; however, chemostats are limited in their scale both in terms of experimental replication (numbers of treatments × replicates) and timescale (long-term contamination free chemostats are challenging to maintain) [12, 13]. These factors limit our understanding of the dynamic interplay between respiration and growth rate, particularly under changing environmental conditions. Recent work showed that asynchronous measurement of respiration and biomass production can distort carbon budgets, systematically overestimating respiration, underestimating growth efficiency, and inflating the apparent role of bacteria in community metabolism [14]. Environmental factors such as temperature, pH, nutrient availability, and osmotic stress influence growth and respiration through distinct physiological mechanisms. As a result, integrated, time-resolved measurements that capture both processes are increasingly essential for understanding microbial energy partitioning. Decoupling between these processes at the cellular level can scale up to affect ecosystem functions such as carbon sequestration, nutrient turnover, and greenhouse gas fluxes [7, 15, 16].

Here we present a method to infer bacterial growth and respiration rate from a single dissolved-oxygen time series. We developed a mathematical model that treats growth as an exponential process and assumes that oxygen uptake is proportional to biomass. We applied our approach to estimate growth and respiration in 15 phylogenetically diverse bacterial strains under standardized laboratory conditions. Growth rates derived from our novel oxygen gradient method were confirmed by independent measurements of growth rate made using flow cytometry and spectrophotometry. To

illustrate its broader utility, we applied our approach to *Pseudomonas* sp. exposed to a controlled thermal gradient, enabling the measurement of temperature-dependent changes in growth, respiration, and carbon use efficiency (CUE) from a single oxygen time series. This unified approach reveals new insights into microbial energy allocation and metabolic flexibility across conditions, offering valuable tools for both basic ecology and applied microbiology.

Materials and methods

Bacterial taxa

Experiments were conducted using 15 heterotrophic bacterial taxa originally isolated from Icelandic geothermal pools [17]. Taxa were identified by 16S rRNA gene sequencing and included *Aeromonas* sp. (strain A and B), *Bacillus* sp., *Pseudomonas* sp., *Flavobacterium* spp. (strain A and B), *Yersinia* sp., *Serratia* sp., *Burkholderia* sp., *Buttiauxella* sp., *Chryseobacterium* sp., *Herbaspirillum* sp., *Arthrobacter* sp., *Chromobacterium* sp., and *Acinetobacter* sp.

Bacterial monoculture preparations

Each bacterial isolate was revived from −80°C glycerol freezer stocks and streaked onto Lysogeny Broth (LB) agar plates. A single colony was then inoculated into sterile LB medium (10 g tryptone, 5 g yeast extract, 10 g NaCl per litre) and incubated at 30°C for 16 h (Panasonic Corporation, Japan). Following incubation, optical density at 600 nm (OD_{600}) was measured by Infinite 200 PRO plate reader (Tecan Life Sciences, Switzerland), and cultures were diluted into fresh, prewarmed, and aerated LB medium to an initial OD_{600} of 0.05. Following a 2-h incubation to promote entry into exponential growth, cultures were further diluted to a final OD_{600} of 0.0005.

Dissolved oxygen measurements

Oxygen consumption was measured using SensorDish® readers (PreSens GmbH, Germany), which enable real-time, noninvasive monitoring of up to 24 samples per plate via optical sensor spots

containing a fluorescent dye quenched by oxygen [18]. The degree of quenching correlates with the oxygen partial pressure, enabling noninvasive, real-time measurement of dissolved oxygen concentrations (PreSens Precision Sensing GmbH., 2025). The system was factory-calibrated prior to use, and before each experimental run, we additionally performed a two-point calibration against 0% and air-saturated oxygen following the manufacturer's protocol, to verify linearity and stability of the sensor response over the range relevant for our assays. Vials were sterile upon first opening, as supplied by the manufacturer, and were handled aseptically throughout. All liquid handling was performed in a sterile laminar flow hood to prevent contamination. Five replicate vials were prepared per strain by aliquoting from the same pregrown culture at OD_{600} = 0.0005. Each 5 ml vial was filled to slight convexity, just above the rim, to eliminate headspace and thereby minimize atmospheric O_2 exchange, then sealed with the manufacturer-supplied gas-tight caps. Vials were placed on the readers in temperature-controlled incubators set to a constant temperature (30°C for the multi-taxon experiment and fixed set points between 20°C and 40°C for the temperature experiment) and incubated for ~45 min to allow the SensorDish® optical signal and baseline to stabilize; during this period, the reported dissolved-oxygen values may drift slightly upward as the reader optics warm up and internal temperature-compensation and calibration routines settle. Dissolved oxygen concentrations were then recorded at 1-min intervals over a ~200-min period.

Optical density and flow cytometry measurements

To obtain flow-cytometry and OD_{600} measurements without opening the SensorDish® vials during the initial stabilization period, we prepared a parallel set of cultures using the same inocula, vials, medium, and handling procedure and incubated them under identical conditions in a separate incubator. This incubator was the same brand and model as the one housing the SensorDish® unit and was set to the same temperature; temperatures in both incubators were monitored regularly and showed no systematic differences. For each taxon, five parallel vials were prepared. After 45 min of incubation (matching the SensorDish® stabilization period),

subsamples were taken from all five parallel vials, fixed immediately, and later quantified by flow cytometry. These measurements provide a taxon-specific reference cell density after the stabilization period that was used to support the OD_{600}/flow-cytometry growth-rate comparisons while keeping the SensorDish® oxygen time series uninterrupted.

In the SensorDish® experiment itself, subsamples were taken at inoculation from each vial and quantified by flow cytometry, and final OD_{600} and flow-cytometry measurements were obtained from the corresponding SensorDish® vials at the end of the run. Together, the parallel-vial measurements (early reference density) and the SensorDish® vial measurements (inoculation and endpoint) were used for method comparisons and for parameterizing the oxygen-based analysis described below (Oxygen-based Model for Simultaneous Estimation of Growth and Respiration section).

Optical density at 600 nm (OD_{600}) was measured using a microplate reader to estimate total biomass. For flow cytometry, 490 μl of culture was mixed with 10 μl of 25% glutaraldehyde (Sigma-Aldrich, USA), incubated at 4°C for 20 min, and then snap-frozen in liquid nitrogen. Samples were stored at -70°C until further analysis. Prior to flow cytometric measurement, samples were thawed at 37°C with shaking at 300 rpm for 5 min, then diluted by mixing 50 μl of thawed culture with 450 μl of sterile phosphate-buffered saline. SYBR Green I (Thermo Fisher Scientific, USA) was used as a nucleic acid stain and added by mixing 2.5 μl of a 100× solution into each 500 μl sample. Samples were incubated in the dark at room temperature for 1 h prior to analysis. A CytoFLEX S flow cytometer (Beckman Coulter, Inc., USA) was used to quantify cell counts. SYBR-stained sterile LB was used as a blank to determine background fluorescence.

Oxygen-based model for simultaneous estimation of growth and respiration

We estimated microbial specific growth rates and per-cell respiration rates from dissolved oxygen (O_2) time series using a mechanistic model that couples exponential population growth with biomass-proportional oxygen consumption. Below, we explicitly derive the model, describe the data preprocessing and fitting

procedure, and define how respiration rates are recovered from fitted parameters.

Model formulation

Let $N(t)$ denote cell density (cells l^{-1}) at time t, and let $O_2(t)$ denote the dissolved oxygen concentration (mg O_2 l^{-1}). Over the fitted time window, we assume exponential population growth,

$$\frac{dN}{dt} = r\,N, \quad N(t) = N_0 e^{rt} \tag{1}$$

where r is the specific growth rate (min^{-1}) and N_0 is the cell density at the start of the fitted oxygen trajectory (t = 0).

We further assume that the instantaneous rate of oxygen consumption is proportional to total biomass, equivalently to cell density, with a constant per-cell respiration rate R (mg O_2 $cell^{-1}$ min^{-1})

$$\frac{dO_2}{dt} = -RN(t). \tag{2}$$

Substituting Eq. (1) into Eq. (2) and integrating from t = 0 yields

$$O_2(t) = O_{2,0} - \frac{RN_0}{r}\left(e^{rt} - 1\right), \tag{3}$$

where $O_{2,0}$ is the oxygen concentration at the start of the fitted trajectory. The composite factor $\frac{RN_0}{r}$ represents the oxygen consumption scale, jointly determined by per-cell respiration, initial cell density, and population growth rate, a physiological quantity that sets the overall magnitude of the decline.

Normalization and re-zeroing]

Prior to model fitting, each oxygen time series was preprocessed to isolate the time interval over which the assumptions of exponential growth and biomass-proportional respiration were most plausible.

First, raw oxygen trajectories were smoothed using a cubic smoothing spline (smooth.spline; spar = 0.40) to suppress high-frequency sensor noise. The smoothed trajectory was used only for identifying inflection points and the onset of sustained oxygen decline; all model fitting was performed on the unsmoothed data.

Second, each series was trimmed to retain only the interval from the local oxygen maximum (the point after which oxygen declines monotonically) to the point at which the magnitude of dO_2/dt began to decrease, operationally defined as the second inflection point of the smoothed trajectory. This removed late-time data in which growth is no longer exponential.

Third, within this trimmed interval, we identified the onset of sustained oxygen decline using the first derivative of the smoothed trajectory and initiated the fitted window after a short buffer (typically 2–3 min) to avoid residual lag-phase effects.

Time was then re-zeroed so that the first retained observation corresponds to t = 0. The elapsed time between inoculation and this point, denoted Δt, was recorded for each replicate.

Finally, oxygen concentrations were normalized by the reference oxygen level

$$O_2(t) = \frac{1}{3}\sum_{i=1}^{3} O_2\,(t_i), \tag{4}$$

the mean of the first three retained observations within the fitted window, chosen to provide a stable reference that is less sensitive to single-point sensor noise while remaining close to the start of the fitted period. The dimensionless normalized oxygen trajectory is therefore

$$O^*(t) = \frac{O_2(t)}{O_{ref}}. \tag{5}$$

This normalization removes small calibration offsets and suppresses artefacts arising from minor sensor drift during

instrument warm-up, ensuring that parameter estimation is driven primarily by trajectory shape.

Normalized model and parameterization

Dividing Eq. (3) by O_{ref} yields

$$O^*(t) = O_0^* - \frac{RN_0}{rO_{ref}}\left(e^{rt} - 1\right), \tag{6}$$

where $O_0^* = O_{2.0}/O_{ref}$ is a dimensionless intercept expected to be close to unity.

We define the initial fractional oxygen decline rate

$$k_{O_2} = -\left.\frac{dO^*}{dt}\right|_{t=0} \tag{7}$$

which, from Eq. (6), satisfies

$$k_{O_2} = \frac{RN_0}{O_{ref}}. \tag{8}$$

Substituting Eq. (8) into Eq. (6) yields the fitted model

$$O^*(t) = O_0^* + \frac{k_{O_2}}{r}\left(1 - e^{rt}\right) \tag{9}$$

in which r controls the curvature of the trajectory and k_{O_2} controls the initial slope. Differentiation of Eq. (9) confirms that $dO^*/\,dt|_{t=0} = -k_{O_2}$.

Model fitting

Equation (9) was fitted independently to each replicate time series using nonlinear least squares (nlsLM, minpack.lm package in R). The fitted parameters were r, k_{O_2}, and O_0^*. Parameter bounds were chosen to exclude nonphysical solutions while remaining intentionally broad:

$10^{-4} \le r \le 10^{-1}\ \mathrm{min}^{-1}$, $10^{-5} \le k_{O_2} \le 5 \times 10^{-1}$, and $0.8 \le O_0^* \le 1.2$.

Goodness of fit was summarized using a pseudo-$R^2 = 1 - \frac{SS_{res}}{SS_{tot}}$, computed on the normalized oxygen values.

Recovery of per-cell respiration

The total oxygen consumed over the fitted window of duration T is

$$C_{\mathrm{tot}} = O_{ref} \frac{k_{O_2}}{r} \left(e^{rT} - 1\right). \tag{10}$$

The time-integrated cell density over the same interval is

$$\int_0^T N(t)\, dt = \frac{N_0}{r} \left(e^{rT} - 1\right). \tag{11}$$

Dividing total oxygen consumption by time-integrated cell density yields the per-cell respiration rate

$$R = \frac{k_{O_2} O_{ref}}{N_0} \tag{12}$$

The initial cell density N_0 was reconstructed from the measured inoculation density N_{inoc} and the recorded delay Δt between inoculation and the start of the fitted oxygen trajectory:

$$N_0 = N_{\mathrm{inoc}}\, e^{r\Delta t} \tag{13}$$

Sensitivity and model validation analyses

In the oxygen model (Eq. 9), the decline in $O^*(t)$ is parameterized by the initial fractional oxygen decline rate k_{O_2}(Eq. 7). Because r is inferred from the curvature of the normalized oxygen trajectory (Eq. 9), the fitted estimate of r is independent of the assumed value of N_0. In contrast, the per-cell respiration rate R is recovered after fitting by combining k_{O_2} with O_{ref} and N_0(Eq. 12). Equivalently, Eq. (12) can

be rearranged to $k_{O_2} = (RN_0)/O_{\text{ref}}$ (from Eq. 8), showing that uncertainty in N_0 propagates directly into R. To quantify this propagation, we performed a Monte Carlo sensitivity analysis (Supplementary Table S1).

Using replicate-specific estimates of N_0(cells l^{-1}) available for each taxon × replicate time series, we treated each replicate's fitted N_0 as the scenario mean $\hat{N}_0$ and explored a grid of assumed coefficients of variation (CV = 0.10, 0.20, 0.30, 0.40) to represent plausible uncertainty in N_0. For each taxon × replicate time series and each CV scenario, we generated $N_{\text{MC}} = 300$ random draws $N_0^{(k)}$ from a lognormal distribution parameterized to have mean $\hat{N}_0$ and standard deviation $\text{CV} \times \hat{N}_0$, ensuring $N_0^{(k)} > 0$. We held the fitted values of k_{O_2} and O_{ref} fixed for that time series and recalculated the per-cell respiration rate for each draw using Eq. (12), substituting $N_0^{(k)}$ for N_0.

For each replicate, we summarized the resulting distribution of $R^{(k)}$ by its relative standard deviation (SD/mean) and additionally extracted the 2.5% and 97.5% quantiles. We then summarized these replicate-level sensitivities at the taxon level (median, minimum, and maximum across replicates) and across all series (overall median, minimum, and maximum).

In addition, we carried out a synthetic-data validation to test whether both r and k_{O_2} (and therefore R) can be reliably recovered from single dissolved-oxygen time series under realistic experimental conditions (Supplementary Fig. S2, Table S2). We generated artificial normalized O_2 trajectories from the oxygen model in Eq. (9), using parameter combinations spanning the empirical range of r and R used in the simulation design. Per-cell respiration was mapped into the fitted model via $k_{O_2} = (RN_0)/O_{\text{ref}}$ (from Eq. 8). These trajectories were sampled at realistic intervals ($\Delta t = 1, 3,$ or 5 min) over time windows up to 180 min, and Gaussian noise was added (SD = 0.002–0.01 in O^* units). To mimic finite usable windows, the simulated series were truncated once O^* fell to 40% of its initial level (if reached); otherwise, the full duration was retained. Each synthetic dataset was then fitted using the same nonlinear least-squares framework ($nlsLM$ with bounded parameters and nontruth starting values), and recovered estimates

of r and k_{O_2} were converted back to per-cell respiration using Eq. (12).

Recovered parameter estimates were compared directly with their known true values, and performance was summarized using bias and Root Mean Square Error (RMSE) across sampling intervals, durations, and noise levels (Table S2).

As an additional robustness check on the fitted window, we re-fitted the same normalized oxygen model using only observations with $O^* \geq 0.5$ (i.e. the upper half of the normalized oxygen range) and compared the resulting estimates of r and k_{O_2} to those obtained from the full trimmed window (Supplementary Table S3).

A visual summary of the experimental pipeline and analytical workflow is provided in Fig. 1. For additional practical guidance on implementing the oxygen-based model, including common pitfalls and recommended solutions, see Supplementary Note S1.

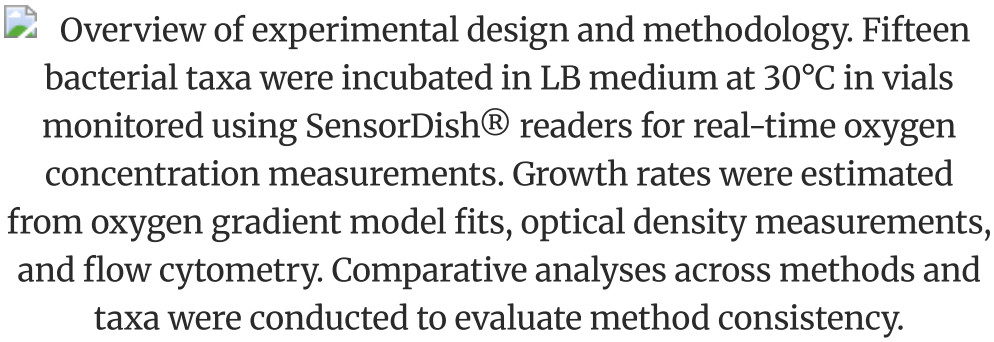

Figure 1 Overview of experimental design and methodology. Fifteen bacterial taxa were incubated in LB medium at 30°C in vials monitored using SensorDish® readers for real-time oxygen concentration measurements. Growth rates were estimated from oxygen gradient model fits, optical density measurements, and flow cytometry. Comparative analyses across methods and taxa were conducted to evaluate method consistency.

Environmental gradient assays and stress response modelling

To investigate metabolic responses under environmental stress, we applied the oxygen-based modelling framework to a single strain of *Pseudomonas* exposed to a controlled temperature gradient. Temperature effects were assessed by incubating cultures at 20°C, 24°C, 28°C, 32°C, 36°C, and 40°C, with four replicates per condition.

Cultures were incubated in sealed vials and monitored at 1-min intervals for ~3 h, so that rapid oxygen dynamics at temperatures deviating from the thermal optimum were captured. The cell density at inoculation (N_{inoc}, cells μl^{-1}) was measured by flow cytometry. The specific growth rate r (min^{-1}) was then estimated from the dissolved-oxygen time series using the nonlinear oxygen model (Eq. 9). Given the known delay Δt between inoculation and the start of the fitted oxygen trajectory, the cell density at the start of the oxygen trajectory (N_0, cells l^{-1}) was projected forward from N_{inoc} assuming exponential growth (Oxygen-based Model for Simultaneous Estimation of Growth and Respiration).

For the estimation of cellular carbon content, cell dimensions were based on *Pseudomonas* sp., described as rod-shaped bacteria measuring 0.5–0.8 μm in diameter and 1.5–3.0 μm in length [19]. The resulting mean cell volume was multiplied by 100 fg C μm^{-3}, which lies at the upper end of values reported for actively growing bacterial cells [20]. Specific growth rates (r, in min^{-1}) were then converted to carbon-based biomass production rates by multiplying r by the initial cell density (cells l^{-1}) and the estimated cellular carbon content (fg C $cell^{-1}$), yielding growth in fg C l^{-1} min^{-1}.

Respiration was estimated by fitting the nonlinear oxygen model (Eq. 9) to normalized oxygen time series, with oxygen scaled by the mean of the first three measurements within the fitted window (O_{ref}; mg $O_2 l^{-1}$). The fitted initial fractional oxygen decline rate k_{O_2}(min^{-1}) was then converted to a volumetric oxygen-consumption rate ($k_{O_2} O_{\mathrm{ref}}$; mg O_2 l^{-1} min^{-1}). For per-cell reporting, the cell density at the start of the fitted oxygen trajectory (N_0) was reconstructed from the inoculation density (N_{inoc}) and the recorded delay between inoculation and the start of the fitted trajectory (Δt) assuming exponential growth ($N_0 = N_{\mathrm{inoc}} e^{r\Delta t}$; Eq. 13), and per-cell respiration was calculated as $R = k_{O_2} O_{\mathrm{ref}} / N_0$ (Eq. 12). Volumetric oxygen-consumption rates were converted to mol O_2 using the molar mass of O_2 (31.998 g mol^{-1}) and then expressed in carbon units, assuming a 1:1 molar ratio between O_2 consumed and C oxidized, using the atomic mass of carbon (12 g mol^{-1}). These stoichiometric assumptions were used only to place growth and respiration on a common carbon scale in the *Pseudomonas* temperature experiment.

CUE was calculated as the ratio of carbon-based biomass production (growth) rate, P, to the sum of biomass production and respiration rate, $P + R$

$$\mathrm{CUE} = \frac{P}{P + R} \tag{14}$$

Data handling & statistical analyses

All statistical analyses were performed in R (version 4.4.3) (R Core Team, 2010). All analysis scripts are available at https://github.com/icakin/OxygenModel. Replicate-level growth rates were first visualized using boxplots grouped by taxon and by method, created with *ggplot2* [21] and *patchwork* [22]. This allowed assessment of both within-taxon variability and global differences across oxygen, OD_{600}, and flow cytometry (FC)–derived estimates. Growth rates from optical density and FC were estimated by calculating the exponential rate of increase between the initial and final timepoints of each replicate:

$$r = \frac{\ln\left(N_{\text{final}}\right) - \ln\left(N_{\text{initial}}\right)}{t_{\text{final}} - t_{\text{initial}}} \tag{15}$$

To evaluate agreement between oxygen-derived growth rates and those estimated from optical density (OD_{600}) and FC, linear mixed-effects models were then applied using *lme4::lmer()* [23].

Bacterial taxon was included as a random intercept in the mixed-effects models to account for baseline differences in growth rates among taxa. This allowed us to test whether a consistent relationship was present across measurement methods while controlling for taxon-specific variation. Fixed-effect slopes were used to quantify the expected change in oxygen-derived growth per unit change in growth rates estimated from either OD_{600} or FC. Model performance was summarized using R^2 computed as the squared correlation between fitted and observed oxygen-derived growth rates. For visualization, replicate-level data were normalized by subtracting taxon-specific random intercepts, using functions from *dplyr* [24] and *tidyr* [25]. This procedure removed baseline

offsets and enabled a clearer comparison of method agreement on a common scale.

To analyse growth–respiration coupling, we expressed both oxygen-derived growth and oxygen-derived respiration in comparable carbon units at the per-cell, per-time scale. Because taxon-specific cell sizes were not measured for all isolates, these conversions are necessarily approximate and are intended for unit harmonization rather than precise taxon-specific biomass estimation. We therefore used a single representative cell volume of 1.0 μm [3] for all taxa and converted this volume to cellular carbon, assuming a carbon density of 100 fg C per μm [3] (i.e. 100 fg C per cell under this convention). Oxygen consumption was converted to carbon respired, assuming a 1:1 molar ratio of O_2 consumed to C respired (i.e. 12/32 mg C per mg O_2). Growth in carbon units was then obtained by multiplying the oxygen-derived specific growth rate by the representative cellular carbon content, while respiration in carbon units was obtained by converting the per-cell oxygen respiration rate to carbon and scaling to the same time basis. These carbon-unit fluxes were used in subsequent mixed-effects analyses of growth–respiration relationships across taxa.

To further assess systematic bias and agreement between methods, we applied Bland–Altman analysis [26]. Bland–Altman plots are widely used to compare two quantitative measurement techniques because they visualize not only the average agreement but also potential biases across the measurement range. For each replicate, the difference between paired measurements was calculated as:

$$d_i = x_i - y_i \tag{16}$$

where x_i is the growth rate estimated from oxygen dynamics and y_i is the corresponding estimate from OD_{600} or FC. The average of the two methods was computed as:

$$m_i = \frac{x_i + y_i}{2} \tag{17}$$

The Bland–Altman plot displays d_i on the y-axis against m_i on the x-axis. The mean difference $\bar{d}$ provides an estimate of systematic

bias between methods. Limits of agreement (LoA) were then calculated as:

$$\mathrm{LoA} = \bar{d} \pm 1.96\ s_d \tag{18}$$

where s_d is the standard deviation of the differences. These limits represent the interval within which 95% of the pairwise differences are expected to fall, thereby quantifying the range of divergence between methods across the observed growth rate spectrum. All analyses were conducted at replicate-level resolution in order to preserve within-taxon variability rather than averaging across replicates.

Growth and respiration rates for the temperature-gradient experiments were estimated by fitting the nonlinear oxygen-consumption model to each replicate using *nlsLM()* from the *minpack.lm* package [27], following the procedure outlined in the Oxygen-based Model for Simultaneous Estimation of Growth and Respiration section. Thermal responses of growth and respiration were then characterized by fitting Sharpe–Schoolfield models to the estimated rates, allowing identification of activation energies and thermal optima [28, 29]. CUE was modelled with an Arrhenius function, reflecting its generally monotonic decline with increasing temperature [30].

Results

Deriving bacterial respiration and growth rate from oxygen time-series

The mechanistic oxygen model closely reproduced the observed oxygen-depletion trajectories across taxa and replicates (Fig. 2), with a median pseudo-R^2 > 0.99. Residuals showed no obvious temporal structure and no strong heteroscedasticity across the fitted window (Supplementary Fig. S1). Estimated growth rates ranged from 0.008 to 0.046 min^{-1}, while per-cell respiration rates ranged from 1.98×10^{-11} to 1.89×10^{-9} mg $O_2\ cell^{-1}\ min^{-1}$, indicating substantial intertaxon variation under standard conditions. Full

fitted trajectories for all five replicates of the 15 taxa are provided in Supplementary Fig. S3.

Taxon-specific oxygen consumption dynamics and model-derived metabolic rates. Dissolved oxygen concentration (mg l–1) over time for 4 representative bacterial taxa (selected from 15 total) under standardized assay conditions. Black dots show observed oxygen concentrations; solid lines represent model fits. The mechanistic model estimated the specific growth rate (r) and the initial normalized oxygen-decline parameter (${k}_{{\mathrm{O}}_2}$) from each dissolved-oxygen time series; per-cell respiration rates (R) were then recovered using Eq. (12) with ${O}_{\mathrm{ref}}$ and replicate-specific ${N}_0$ and reported within each panel.

Figure 2 Taxon-specific oxygen consumption dynamics and model-derived metabolic rates. Dissolved oxygen concentration (mg l^{-1}) over time for 4 representative bacterial taxa (selected from 15 total) under standardized assay conditions. Black dots show observed oxygen concentrations; solid lines represent model fits. The mechanistic model estimated the specific growth rate (r) and the initial normalized oxygen-decline parameter (k_{O_2}) from each dissolved-oxygen time series; per-cell respiration rates (R) were then recovered using Eq. (12) with O_{ref} and replicate-specific N_0 and reported within each panel.

Validating the modelling pipeline

To quantify the effect of uncertainty in N_0 on per-cell respiration (R), we perturbed N_0 while holding r, k_{O_2}, and O_{ref} fixed (Supplementary Table S1). Across 75 time series, uncertainty in R increased in near 1:1 proportion to the imposed uncertainty in N_0: the median relative standard deviation of R was 0.100, 0.199, 0.299, and 0.399 for 10%, 20%, 30%, and 40% CV in N_0, respectively, with modest between-series variation (e.g. 0.093–0.109 at 10% CV; Supplementary Table S1). Estimates of r were unchanged by N_0 perturbation (Eq. 9) because r is identified from the curvature of the O_2 trajectory.

Next, we validated parameter recovery using synthetic oxygen time series generated from Eq. (9) and whether recovered k_{O_2} values can be converted back to R when N_0 is known (Eq. 12). Synthetic data were generated from the model across realistic parameter ranges,

with Gaussian observation noise (SD = 0.002–0.01 in normalized O_2 units), sampling intervals (1–5 min), and durations (60–180 min). Across all conditions (450 fits per setting), the pipeline recovered parameters with small bias (typically <1% relative bias; worst-case $\sim$ 2% for r under the highest noise and shortest duration) and high overall curve-fit quality (mean pseudo-R^2 = 0.990–0.999; Supplementary Table S2). Precision decreased systematically with increasing noise and shorter time series, with RMSE for r ranging from $\sim 2 \times 10^{-4}$ to $\sim 3 \times 10^{-3}$ across the explored conditions.

Finally, we assessed sensitivity to the fitted time window by repeating model fitting using only the early portion of each oxygen time series, truncated at the time when normalized oxygen first declined to 0.5 of its initial value (the '0.5' window). Estimates from the reduced window ($r_{0.5}, k_{O_{2_{0.5}}}$) closely matched the main estimates ($r_{main}, k_{O_{2_{main}}}$), with typical deviations $\lesssim$1% across taxa and replicates (Supplementary Table S3).

Comparison of growth rate estimates across measurement methods

Growth rate estimates obtained from the oxygen-based model were highly consistent with those derived from conventional approaches, including optical density (OD_{600}) and flow cytometry (FC), across all 15 bacterial taxa tested (Fig. 3). Oxygen-derived estimates spanned a very similar range to OD_{600}- and FC-based measurements, and distributions across taxa showed comparable medians and variability.

Comparison of bacterial growth rate estimates across methods. Growth rates (per minute) were estimated using three independent methods: oxygen consumption modelling, optical density at 600 nm (OD6₀₀), and flow cytometry. The left panel shows method-specific growth rate distributions for each of the 15 bacterial taxa. Each boxplot represents replicate-level estimates, with horizontal lines indicating the median and whiskers denoting the interquartile range.

Figure 3 Comparison of bacterial growth rate estimates across methods. Growth rates (per minute) were estimated using three independent methods: oxygen consumption modelling, optical density at 600 nm (OD_{600}), and flow cytometry. The left panel shows method-specific growth rate distributions for each of the 15 bacterial taxa. Each boxplot represents replicate-level estimates, with horizontal lines indicating the median and whiskers denoting the interquartile range.

Some taxon-specific deviations were evident, with oxygen-based estimates occasionally higher or lower than those from OD_{600} or FC, but these differences varied in direction across taxa and did not indicate systematic bias. When estimates were pooled across taxa, the three methods yielded nearly identical distributions. Visual patterns were supported by statistical analysis. A mixed-effects ANOVA with 'method' as a fixed effect and 'taxon' as a random intercept detected no significant overall effect of method, as a likelihood ratio test comparing models with and without method terms confirmed (x^2 = 2.60, df = 2, P = .27). Pairwise contrasts with Bonferroni correction likewise indicated no significant differences among oxygen-, OD_{600}-, and FC–derived growth rates (all *n*s).

To quantitatively compare growth rate estimates derived from oxygen consumption with those obtained via OD_{600} and FC, we fitted linear mixed-effects models incorporating taxon as a random intercept. The oxygen-derived growth rate was used as the response variable, and either the OD_{600}- or FC-derived growth rate was used as the predictor. Oxygen-based estimates showed a strong linear relationship with OD_{600}-based growth rates (R^2 = 0.943), with a fixed-effect slope of 0.913 (95% CI: 0.764–1.062) and an intercept of 0.003 (Fig. 4A). The relationship between oxygen- and FC-derived growth rates was similarly strong (R^2 = 0.968), with a slope of 0.887 (95% CI: 0.817–0.957) and an intercept of 0.003 (Fig. 4B).

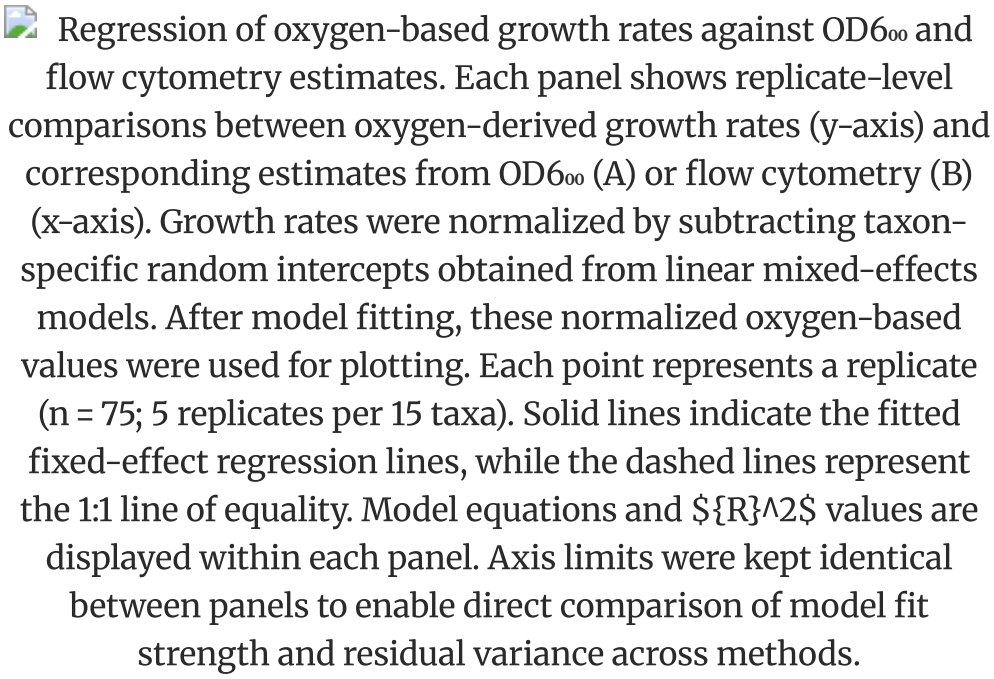

Figure 4 Regression of oxygen-based growth rates against OD_{600} and flow cytometry estimates. Each panel shows replicate-level comparisons between oxygen-derived growth rates (*y*-axis) and corresponding estimates from OD_{600} (A) or flow cytometry (B) (*x*-axis). Growth rates were normalized by subtracting taxon-specific random intercepts obtained from linear mixed-effects models. After model fitting, these normalized oxygen-based values were used for plotting. Each point represents a replicate ($n = 75$; 5 replicates per 15 taxa). Solid lines indicate the fitted fixed-effect regression lines, while the dashed lines represent the 1:1 line of equality. Model equations and R^2 values are displayed within each panel. Axis limits were kept identical between panels to enable direct comparison of model fit strength and residual variance across methods.

Agreement between oxygen-based and reference methods was evaluated using Bland–Altman analysis [31] (Fig. 5). For OD_{600}-based growth rates (Fig. 5A), oxygen estimates showed a mean bias of 0.001 min^{-1}, with 92.0% of replicate values falling within the limits of agreement (−0.007 to 0.009 min^{-1}). Mixed-effects regression within these limits indicated no evidence of proportional bias (slope = 0.114, R^2 = 0.685, P = .112). Comparisons with flow cytometry yielded similar results (Fig. 5B), with a mean bias of 0.000 min^{-1} and 97.3% of values within the limits of agreement (−0.004 to 0.005 min^{-1}). The corresponding regression also showed no significant proportional bias (slope = −0.034, R^2 = 0.592, P = .365).

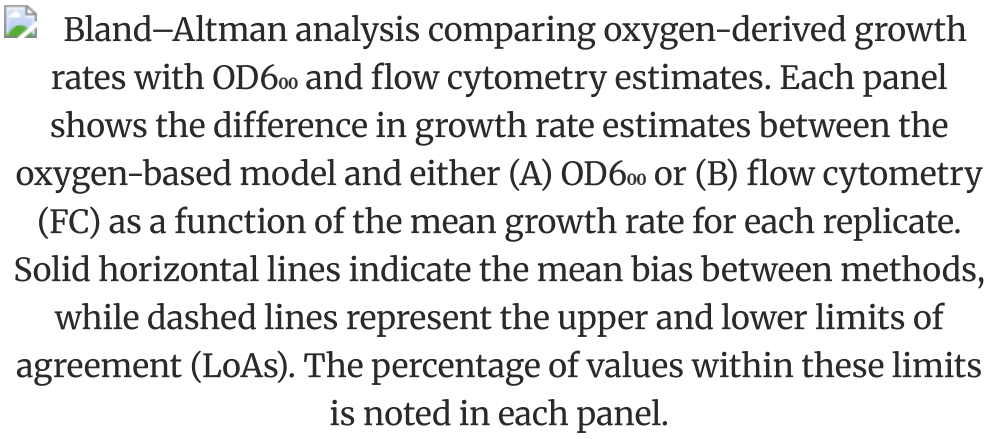

Figure 5 Bland–Altman analysis comparing oxygen-derived growth rates with OD_{600} and flow cytometry estimates. Each panel shows the difference in growth rate estimates between the oxygen-based model and either (A) OD_{600} or (B) flow cytometry (FC) as a function of the mean growth rate for each replicate. Solid horizontal lines indicate the mean bias between methods, while dashed lines represent the upper and lower limits of agreement (LoAs). The percentage of values within these limits is noted in each panel.

Cross-taxon coupling between respiration and growth

To test whether respiration and growth covary across taxa while accounting for taxon-level differences, we fitted a linear mixed-effects model relating log10-transformed, per-cell carbon-based growth rate (fg C $cell^{-1}$ h^{-1}) to log10-transformed, per-cell carbon-based respiration rate (fg C $cell^{-1}$ h^{-1}), with taxon included as a random intercept and random slope to allow both baseline offsets among taxa and taxon-specific growth–respiration sensitivities. Across replicates, growth increased with respiration (fixed-effect intercept = 1.47, slope = 0.19; Fig. 6). Model predictions closely tracked the observed values (R [2] for observed vs. model-predicted = 0.87), indicating a strong across-taxon association between higher per-cell respiration and higher per-cell growth when expressed in harmonized carbon units.

Association between per-cell respiration carbon flux (${R}_{\mathrm{C}}$; fg C cell–1 h–1) and per-cell growth carbon flux (${G}_{\mathrm{C}}$; fg C cell–1 h–1) across all replicates and taxa, plotted on base-10 logarithmic axes. ${R}_{\mathrm{C}}$ was obtained by converting per-cell oxygen respiration rates to carbon units, assuming a 1:1 molar ratio of O_2 consumed to C respired (12/32 mg C per mg O_2). ${\mathrm{G}}_{\mathrm{C}}$ was calculated by converting oxygen-derived specific growth rates to carbon production using a constant cellular carbon content of 100 fg C per cell. (A) For visualization, values were ‘taxon-collapsed’ by removing taxon-specific baseline offsets (random intercepts) so that taxa can be compared on a common reference scale while retaining taxon-specific slopes; this transformation is for plotting only and does not affect the underlying mixed-effects model fit. Points are individual replicates coloured by taxon. Coloured lines are the taxon-specific fitted relationships from the mixed-effects model with random intercepts and slopes by taxon. The black line shows the fixed-effect regression, and the grey band indicates the 95% confidence interval. (B) Taxon-specific slope estimates (±95% confidence intervals) from the same mixed-effects model (one slope per taxon). Colours match (A). The vertical dashed line indicates the fixed-effect slope.

Figure 6 Association between per-cell respiration carbon flux (R_{C}; fg C cell^{-1} h^{-1}) and per-cell growth carbon flux (G_{C}; fg C cell^{-1} h^{-1}) across all replicates and taxa, plotted on base-10 logarithmic axes. R_{C} was obtained by converting per-cell oxygen respiration rates to carbon units, assuming a 1:1 molar ratio of O_2 consumed to C respired (12/32 mg C per mg O_2). $\mathrm{G_C}$ was calculated by converting oxygen-derived specific growth rates to carbon production using a constant cellular carbon content of 100 fg C per cell. (A) For visualization, values were ‘taxon-collapsed’ by removing taxon-specific baseline offsets (random intercepts) so that taxa can be compared on a common reference scale while retaining taxon-specific slopes; this transformation is for plotting only and does not affect the underlying mixed-effects model fit. Points are individual replicates coloured by taxon. Coloured lines are the taxon-specific fitted relationships from the mixed-effects model with random intercepts and slopes by taxon. The black line shows the fixed-effect regression, and the grey band indicates the 95% confidence interval. (B) Taxon-specific slope estimates (±95% confidence intervals) from the same mixed-effects model (one slope per taxon). Colours match (A). The vertical dashed line indicates the fixed-effect slope.

Importantly, taxa differed in the strength of this coupling: the taxon-specific slopes varied around the global fixed-effect slope (Fig. 6B), indicating that some taxa gained relatively more growth per proportional increase in respiration than others. This variation is consistent with taxon-specific differences in growth efficiency (i.e. the amount of biomass production achieved per unit respiratory carbon flux) under the assay conditions.

Temperature modulation of respiration–growth trade-offs

To quantify temperature effects on microbial energy allocation, we applied our unified respiration–growth model (Eq. 9) to oxygen time series data from *Pseudomonas* sp. exposed to a controlled thermal gradient. Using this framework, we estimated r and k_{O_2} from each oxygen time series and recovered per-cell respiration rates (R) using Eq. (12). We then calculated CUE from carbon-based growth and respiration (Eq. 14), treating CUE as the fraction of total carbon demand allocated to biomass production (Fig. 7). Trait–temperature curves were fitted with Sharpe–Schoolfield models for growth and respiration, and the Arrhenius model for CUE, providing activation energies and thermal optima [30, 32].

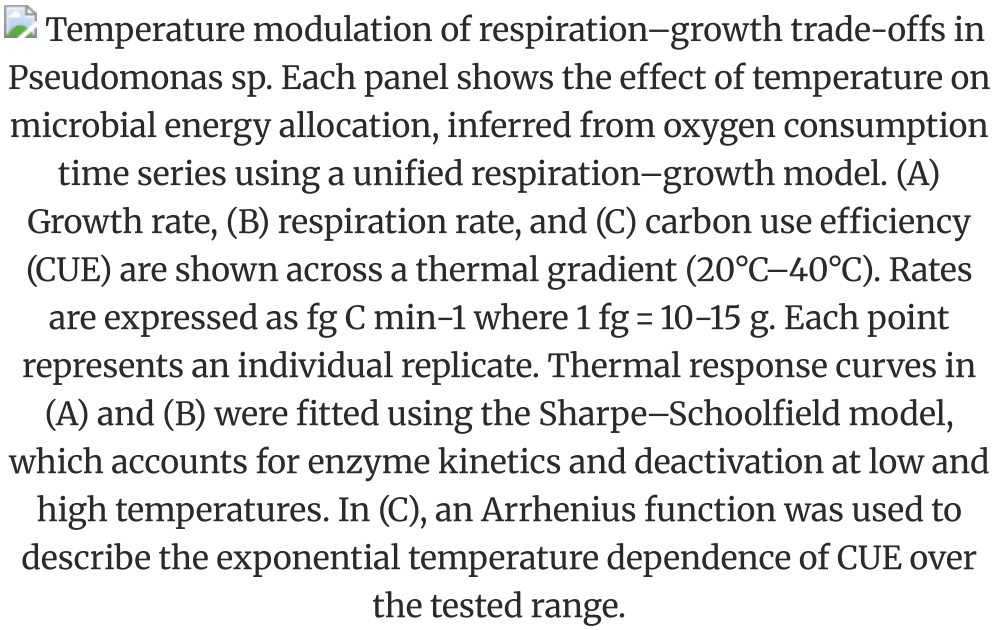

Figure 7 Temperature modulation of respiration–growth trade-offs in *Pseudomonas* sp. Each panel shows the effect of temperature on microbial energy allocation, inferred from oxygen consumption time series using a unified respiration–growth model. (A) Growth rate, (B) respiration rate, and (C) carbon use efficiency (CUE) are shown across a thermal gradient (20°C–40°C). Rates are expressed as fg C min^{-1} where 1 fg = 10^{-15} g. Each point represents an individual replicate. Thermal response curves in (A) and (B) were fitted using the Sharpe–Schoolfield model, which accounts for enzyme kinetics and deactivation at low and high temperatures. In (C), an Arrhenius function was used to describe the exponential temperature dependence of CUE over the tested range.

Growth rates peaked at intermediate temperatures (T_{opt} = 33.9°C) (Fig. 7A), while respiration rates remained elevated at higher temperatures (Fig. 7B; T_{opt} = 37.5°C). The activation energies of growth (0.63 eV, 95% CI 0.57–0.69) and respiration (0.71 eV, 95% CI 0.59–0.84) overlapped, indicating comparable temperature sensitivities, even though respiration peaked at a slightly higher temperature than growth. CUE increased modestly between 20°C and ~30°C, remained relatively high up to ~34°C, and then declined sharply at 40°C (Fig. 7C).

Discussion

Our results demonstrate that high-resolution oxygen consumption data can be used to estimate bacterial growth and respiration rates simultaneously in diverse bacterial taxa, with strong agreement to

independent methods. This provides a practical advance because respiration and growth, two of the most fundamental microbial processes, are rarely quantified together from a single, noninvasive assay. By combining growth and respiration within a single analytical pipeline, our framework resolves energy uptake and biomass generation simultaneously and continuously, unlike conventional approaches that rely on parallel assays, often at mismatched temporal resolution [14, 33] and under different physical–chemical conditions. The approach was repeatable across taxa and replicate vials and produced stable parameter estimates.

A key test of the framework is whether our oxygen-based growth estimates agree with independent methods. Growth estimates from the oxygen method showed strong correlation with both flow cytometry and optical density (OD_{600}) estimates. The high correlation ($R^2 > 0.9$), low bias, and tight limits of agreement in Bland–Altman plots support congruence between oxygen-based growth estimates and conventional methods. Minor differences between methods were taxon-specific and represented the individual sensitivities of optical, cytometric, and oxygen-based methods (Fig. 3). In particular, slopes slightly below unity (Fig. 4) could reflect several factors, including modest overestimation of growth by OD- and FC-based methods [34, 35], whereas flow cytometry may count dye-bound DNA from debris or dead/membrane-compromised cells [36, 37]. Our oxygen-based model provides an indirect yet integrated view of metabolic performance and is especially useful for detecting relative differences in microbial traits when biomass production and energy demand diverge. At the same time, agreement among methods does not, by itself, guarantee that the inferred r is completely free of bias, because OD_{600}, flow-cytometry, and O_2-based estimates could in principle all be affected by the same deviations from idealised exponential growth (e.g. incipient stationary phase). We therefore interpret the cross-method concordance as strengthening confidence in the O_2-based estimates rather than as absolute proof of their ‘correctness’. Notably, no proportional bias was detected, indicating that concordance between methods is consistent across the full range of growth rates observed.

Independent of methodological considerations, the results highlight distinct ecological patterns in bacterial metabolism. The observed

range in growth and respiration strategies suggests bacterial taxa span a spectrum from rapidly growing, energetically demanding phenotypes to slower-growing, low-maintenance organisms [38–40] (see Fig. 6). This spectrum reflects fundamental life-history trade-offs, directly linking cellular physiology to ecosystem-level processes such as carbon flux partitioning between biomass and respiration. By mechanistically quantifying these traits, our framework provides a pathway to embed microbial physiology into predictive ecosystem models in a way that is both scalable and ecologically realistic.

To demonstrate how the framework can be used to study environmental drivers of microbial metabolism, we applied the method to *Pseudomonas* sp. grown across a 20°C–40°C temperature range. We found that the growth rate was optimal at 33.9°C, whereas respiration rates continued to rise to higher temperatures (see Fig. 7). Consequently, CUE rose gradually up to the optimum temperature and then declined rapidly at high temperature, when respiration rates were high relative to the growth rate. These results show how elevated respiration decouples from biosynthesis under heat stress [41]. By measuring growth and respiration simultaneously from the same oxygen trace, the results suggest that maintenance and repair costs increase relative to biosynthetic capacity under heat stress, diverting more energy away from biomass synthesis [42].

We emphasize that this temperature-response analysis is best viewed as a proof-of-concept application of the oxygen-based framework rather than a comprehensive description of bacterial thermal physiology. Although the temperature response of CUE aligns with earlier findings, the exact threshold, shape, and magnitude of the temperature response will likely differ among taxa with distinct metabolic strategies and thermal niches [32]. These insights from a single model strain connect cellular energetics with functional traits that are important for determining climate-sensitive ecosystem processes and illustrate how the methodology could, in future, be used to quantify microbial responses to warming in a high-throughput manner [43]. This approach could also be applied to investigate other stressors such as osmotic pressure or pH changes, providing a more nuanced view of microbial energy budgeting under changing environmental conditions [44, 45]. More broadly, extending this approach to multiple strains and natural

communities will be necessary to characterize the diversity of microbial thermal responses using this novel high-throughput method.

The temperature gradient experiment required expressing growth and respiration in common carbon units, for which we assumed a 1:1 molar O_2:C ratio and a cellular carbon density of 100 fg C μm^{-3}. These values are widely used first-order approximations for aerobic respiration of moderately oxidized substrates and for actively growing bacterial cells, but we acknowledge that both O_2:C stoichiometry and cellular carbon content can vary among taxa, substrates, and growth phases. As a result, the absolute carbon fluxes we report for *Pseudomonas* sp. should be interpreted as order-of-magnitude estimates rather than precise stoichiometric measurements. Our main conclusions for the temperature experiment focus on relative responses (how growth, respiration, and CUE change with temperature) rather than on absolute flux magnitudes; moderate shifts in the assumed O_2:C ratio or carbon density would primarily rescale production and respiration and slightly shift CUE values but are unlikely to overturn the qualitative thermal responses we describe. Future applications could incorporate taxon-specific stoichiometry or formal sensitivity analyses where such information is available.

Several lines of evidence suggest that the patterns we infer are robust to modelling choices and physical confounders. A flexible three-parameter nonlinear function can, in principle, fit many smooth depletion trajectories, so good visual agreement alone does not guarantee that growth and respiration truly remained constant over the full fitting window. Our confidence in the inferred r and R therefore comes from a broader set of checks rather than curve flexibility per se. Synthetic-data tests show that, under realistic noise levels and sampling schemes, the model reliably recovers both r and R with very low bias (Supplementary Table S2). Consistent with this, the near-perfect agreement between estimates obtained from the standard exponential-decline window and those derived when fits are restricted to high-oxygen data (normalized $O_2 \geq 0.5$) indicates that potential low-O_2 limitation has negligible influence on inferred growth and respiration rates (Supplementary Table S3). Because N_0 enters only when converting the fitted oxygen-decline parameter k_{O_2} into per-cell respiration R (Eq. 12) and does not

appear in the oxygen time-series model used to estimate r, uncertainty in N_0 primarily affects the absolute scale of respiration rather than the inferred growth rate (Supplementary Table S1). As all oxygen measurements were conducted at constant temperature in headspace-free, gas-tight vials, we expect temperature-driven changes in gas solubility or slow oxygen exchange with the atmosphere to be minimal. The smooth, monotonic depletion curves and highly consistent trajectories across replicate vials are therefore consistent with microbial respiration rather than physical artefacts such as leakage or pressure-induced oxygen flux. Future studies could refine the current assumptions, e.g. by using dynamic yield coefficients or explicitly modelling stress-related respiration costs [46], to explore regimes where deviations from exponential growth become more pronounced.

Moreover, combining this oxygen-centric approach with complementary techniques such as CO_2 flux analysis, isotopic tracers, or single-cell methods would provide a multidimensional view of microbial energy use, pushing the field closer to a systems-level understanding of metabolism [47–49] Overall, we present a scalable system for assessing core microbial metabolic properties using oxygen time series data. By unifying respiration and growth into a single framework, we offer a powerful tool for trait-based microbial ecology, with applications from laboratory phenotyping to ecosystem-scale carbon cycling. Our framework provides a scalable way to link microbial physiology with ecosystem science, supporting high-throughput, trait-based mapping of microbial metabolism and offering a practical link for predicting microbial contributions to carbon cycling under a changing climate.

Conclusions

We present a novel methodological framework that simultaneously estimates bacterial growth and respiration from a single oxygen time series, enabling time-resolved, noninvasive quantification of microbial metabolism. Validated across phylogenetically diverse taxa, the method produced growth estimates consistent with optical density and flow cytometry, demonstrating both congruence with existing methods and broad taxonomic applicability. Critically, by uniting growth and respiration within a single analytical

framework, this approach enables direct quantification of their dynamic interaction under controlled conditions, a capability rarely achieved with existing methods.

Application of this framework to a thermal gradient experiment with *Pseudomonas* sp. revealed systematic shifts in respiration-to-growth ratios, demonstrating the method's capacity to resolve changes in metabolic efficiency along environmentally relevant gradients. These findings illustrate how the approach can detect physiological trade-offs that may be obscured when growth and respiration are measured independently.

This scalable, high-throughput approach enhances microbial phenotyping by providing integrated metabolic profiles, strengthening trait-based ecology by enabling direct measurement of coupled metabolic processes. As microbial processes become increasingly recognized as central to climate-biosphere feedbacks [50], such integrative approaches will be essential for embedding mechanistic microbial function into next-generation Earth system models. By quantifying the linkages between growth and respiration across environmental gradients, this framework provides a pathway toward more realistic representations of microbial contributions to global biogeochemical cycles.

Acknowledgements

We are grateful to the staff of the Living Systems Institute for their help and support.

Author contributions

Ilgaz Cakin (Conceptualization, Methodology, Software, Validation, Investigation, Formal analysis, Resources, Data curation, Writing—original draft), Rebecca Millington (Conceptualization, Methodology, Software, Writing—reviewing and editing), Samraat Pawar (Conceptualization, Resources, Supervision, Funding acquisition), Angus Buckling (Conceptualization, Resources, Supervision, Funding acquisition), Nicholas Smirnoff (Conceptualization, Resources, Supervision, Funding acquisition), Daniel Padfield

(Conceptualization, Resources, Supervision, Funding acquisition), John Duffy (Validation, Resources), Gabriel Yvon-Durocher (Conceptualization, Methodology, Software, Validation, Resources, Writing—reviewing and editing, Supervision, Funding acquisition)

Conflicts of interest

The authors declare no conflict of interest.

Funding

This work was supported by UK Research and Innovation (UKRI) under research grant NE/Y000889/1.

Ethics of research statement

The authors declare that this research paper adheres to the high ethical standards of ISME in conducting and reporting the study. All experimental procedures were carried out in accordance with relevant ethical guidelines and regulations.

Data availability

The authors confirm that the data supporting the findings of this study are available within the article and its Supplementary Material. Raw data that support the findings of this study are available from the corresponding author (i.cakin@exeter.ac.uk), upon request.

Declaration of generative AI and AI-assisted technologies in the writing process

The authors declare that they have not used any of the generative AI and AI-assisted technologies in this research paper.

References

1. Metze D. et al. Microbial growth under drought is confined to distinct taxa and modified by potential future climate conditions. *Nat Commun* 2023;14:5895.
Google Scholar Crossref PubMed WorldCat

2. Fierer N, Lennon JT. The generation and maintenance of diversity in microbial communities. *Am J Bot* 2011;98:439–48.
Google Scholar Crossref PubMed WorldCat

3. McCallister SL, Guillemette F, Del Giorgio PA. A system to quantitatively recover bacterioplankton respiratory CO2 for isotopic analysis to trace sources and ages of organic matter consumed in freshwaters. *Limnol Oceanogr Methods* 2006;4:406–15.
Google Scholar Crossref WorldCat

4. Xu J, Li X, Shi Z. et al. Bacterial carbon cycling in the river plume in the northern South China Sea during summer. *J Geophys Res Oceans* 2018;123:8106–21.
Google Scholar Crossref WorldCat

5. Shi Z, Xu J, Li X. et al. Links of extracellular enzyme activities, microbial metabolism, and community composition in the river-impacted coastal waters. *J Geophys Res Biogeosci* 2019;124:3507–20.
Google Scholar Crossref WorldCat

6. Pirt SJ. The maintenance energy of bacteria in growing cultures. *Proc R Soc Lond B Biol Sci* 1965;163:224–31.
Google Scholar Crossref PubMed WorldCat

7. Russell JB, Cook GM. Energetics of bacterial growth: balance of anabolic and catabolic reactions. *Microbiol Rev* 1995;59:48–62.
Google Scholar Crossref PubMed WorldCat

8. Shuter B. A model of physiological adaptation in unicellular algae. *J Theor Biol* 1979;78:519–52.
Google Scholar Crossref PubMed WorldCat

9. J. Geider R, Osborne BA. Respiration and microalgal growth: a review of the quantitative relationship between dark respiration and growth. *New Phytol* 1989;112:327–41.
Google Scholar Crossref WorldCat

10. Monod J. Recherches Sur la croissance des cultures bactériennes. *Actualités Scientifiques et Industrielles*, vol. 911, pp. 1–210. Paris: Hermann, 1958.
Google Scholar WorldCat

11. Warkentin M, Freese HM, Karsten U. et al. New and fast method to quantify respiration rates of bacterial and plankton communities in freshwater ecosystems by using optical oxygen sensor spots. *Appl Environ Microbiol* 2007;73:6722–9.
Google Scholar Crossref PubMed WorldCat

12. Miller AW, Befort C, Kerr EO, Dunham MJ. Design and use of multiplexed chemostat arrays. *J Vis Exp* 2013;e50262. 10.3791/50262
Crossref

13. Plouchart D, Milferstedt K, Guizard G. et al. Multiplexed chemostat system for quantification of biodiversity and ecosystem functioning in anaerobic digestion. *PLoS One* 2018;13:e0193748.
10.1371/journal.pone.0193748
Google Scholar Crossref PubMed WorldCat

14. Guo C, Ke Y, Chen B. et al. Making comparable measurements of bacterial respiration and production in the subtropical coastal waters. *Mar Life Sci Technol* 2022;4:414–27.
Google Scholar Crossref PubMed WorldCat

15. Knapp BD, Huang KC. The effects of temperature on cellular physiology. *Annu Rev Biophys* 2022;51:499–526.
Google Scholar Crossref PubMed WorldCat

16. Laye VJ, Solieva S, Voelz VA. et al. Effects of salinity and temperature on the flexibility and function of a polyextremophilic enzyme. *Int J Mol Sci* 2022;23:15620.
Google Scholar Crossref PubMed WorldCat

17. García FC, Bestion E, Warfield R. et al. Changes in temperature alter the relationship between biodiversity and ecosystem functioning. *Proc Natl Acad Sci USA* 2018;115:10989–94.
Google Scholar Crossref PubMed WorldCat

18. Werner J, Belz M, Klein K-F, Sun T, Grattan KTV. Fiber optic sensor designs and luminescence-based methods for the detection of oxygen and pH measurement. *Measurement* 2021;178:109323.
10.1016/j.measurement.2021.109323
Crossref

19. Moore NM, Flaws ML. Introduction: pseudomonas aeruginosa. *Clin Lab Sci* 2011;24:41–2. 10.29074/ascls.24.1.41
Google Scholar Crossref PubMed WorldCat

20. Braun S. et al. Size and carbon content of sub-seafloor microbial cells at Landsort Deep, Baltic Sea. *Front Microbiol* 2016;7:1375.
Google Scholar PubMed WorldCat

21. Wickham, H. & Sievert, C. *Ggplot2: Elegant Graphics for Data Analysis*. 10 (springer New York, 2009). 10.1007/978-0-387-98141-3.
Google Scholar Crossref Google Preview WorldCat COPAC

22. Pedersen TL. patchwork: The Composer of Plots. R package version [4.3.1]. CRAN; 2019. 10.32614/CRAN.package.patchwork
Crossref

23. Bates D, Mächler M, Bolker B. et al. Fitting linear mixed-effects models using lme4. *J Stat Softw* 2015;67:1–48.
Google Scholar Crossref WorldCat

24. Wickham H. Dplyr: a grammar of data manipulation. *R package version 04* 2015;3:p156.
Google Scholar WorldCat

25. Wickham H, Vaughan D, Girlich M. tidyr: Tidy Messy Data. R package version 1.3.0. Comprehensive R Archive Network (CRAN); 2023.
10.32614/CRAN.package.tidyr
Crossref

26. Bland JM, Altman D. Statistical methods for assessing agreement between two methods of clinical measurement. *Lancet* 1986;327:307–10.
Google Scholar Crossref WorldCat

27. Elzhov TV, Mullen KM, Spiess A-N, Bolker B. minpack.lm: R Interface to the Levenberg–Marquardt Nonlinear Least-Squares Algorithm Found in MINPACK, Plus Support for Bounds. R package version [4.3.1]. Comprehensive R Archive Network (CRAN); 2016.
10.32614/CRAN.package.minpack.lm
Crossref

28. Schoolfield RM, Sharpe PJH, Magnuson CE. Non-linear regression of biological temperature-dependent rate models based on absolute reaction-rate theory. *J Theor Biol* 1981;88:719–31.
Google Scholar Crossref PubMed WorldCat

29. Garcia FC, Warfield R, Yvon-Durocher G. Thermal traits govern the response of microbial community dynamics and ecosystem functioning to warming. *Front Microbiol* 2022;13:906252.
Google Scholar Crossref PubMed WorldCat

30. Padfield D, Yvon-Durocher G, Buckling A. et al. Rapid evolution of metabolic traits explains thermal adaptation in phytoplankton. *Ecol Lett* 2016;19:133–42.
Google Scholar Crossref PubMed WorldCat

31. Mansournia MA, Waters R, Nazemipour M. et al. Bland-Altman methods for comparing methods of measurement and response to criticisms. *Glob Epidemiol* 2021;3:100045.
Google Scholar Crossref PubMed WorldCat

32. Smith TP, Clegg T, Bell T. et al. Systematic variation in the temperature dependence of bacterial carbon use efficiency. *Ecol Lett* 2021;24:2123–33.
Google Scholar Crossref PubMed WorldCat

33. Lee CW, Bong CW, Hii YS. Temporal variation of bacterial respiration and growth efficiency in tropical coastal waters. *Appl Environ Microbiol* 2009;75:7594–601.
Google Scholar Crossref PubMed WorldCat

34. Dalgaard P, Ross T, Kamperman L. et al. Estimation of bacterial growth rates from turbidimetric and viable count data. *Int J Food Microbiol* 1994;23:391–404.
Google Scholar Crossref PubMed WorldCat

35. Koch AL. Turbidity measurements of bacterial cultures in some available commercial instruments. *Anal Biochem* 1970;38:252–9.
Google Scholar Crossref PubMed WorldCat

36. Zacharias N, Kistemann T, Schreiber C. Application of flow cytometry and PMA-qPCR to distinguish between membrane intact and membrane compromised bacteria cells in an aquatic milieu. *Int J Hyg Environ Health* 2015;218:714–22.
Google Scholar Crossref PubMed WorldCat

37. Emerson JB, Adams RI, Román CMB. et al. Schrödinger's microbes: tools for distinguishing the living from the dead in microbial ecosystems. *Microbiome* 2017;5:86. 10.1186/s40168-017-0285-3
Google Scholar Crossref PubMed WorldCat

38. Weissman JL, Hou S, Fuhrman JA. Estimating maximal microbial growth rates from cultures, metagenomes, and single cells via codon usage patterns. *Proc Natl Acad Sci* 2021;118:e2016810118. 10.1073/pnas.2016810118
Google Scholar Crossref PubMed WorldCat

39. Roller BRK, Schmidt TM. The physiology and ecological implications of efficient growth. *ISME J* 2015;9:1481–7.
Google Scholar Crossref PubMed WorldCat

40. Wang J. et al. Fertilization treatments affect soil CO2 emission through regulating soil bacterial community composition in the semiarid loess plateau. *Sci Rep* 2022;12:20123.
Google Scholar Crossref PubMed WorldCat

41. Apple JK, Del Giorgio PA, Kemp WM. Temperature regulation of bacterial production, respiration, and growth efficiency in a temperate salt-marsh estuary. *Aquat Microb Ecol* 2006;43:243–54.
Google Scholar Crossref WorldCat

42. Kempes CP. et al. Drivers of bacterial maintenance and minimal energy requirements. *Front Microbiol* 2017;8:31.
Google Scholar Crossref PubMed WorldCat

43. Sinsabaugh RL, Manzoni S, Moorhead DL. et al. Carbon use efficiency of microbial communities: stoichiometry, methodology and modelling. *Ecol Lett* 2013;16:930–9.
Google Scholar Crossref PubMed WorldCat

44. Jin Q, Kirk MF. pH as a primary control in environmental microbiology: 1. Thermodynamic perspective. Frontiers in environmental. *Science* 2018;6:21 Preprint at.
Google Scholar WorldCat

45. Wood JM. Bacterial responses to osmotic challenges. *J Gen Physiol* 2015;145:381.
Google Scholar Crossref PubMed WorldCat

46. Schimel J, Balser TC, Wallenstein M. Microbial stress-response physiology and its implications for ecosystem function. *Ecology* 2007;88:1386–94.
Google Scholar Crossref PubMed WorldCat

47. Canarini A. et al. Quantifying microbial growth and carbon use efficiency in dry soil environments via 18O water vapor equilibration. *Glob Chang Biol* 2020;26:5333–41.
Google Scholar Crossref PubMed WorldCat

48. Musat N, Musat F, Weber PK. et al. Tracking microbial interactions with NanoSIMS. *Curr Opin Biotechnol* 2016;41:114–21.
Google Scholar Crossref PubMed WorldCat

49. He X. et al. Emerging multiscale insights on microbial carbon use efficiency in the land carbon cycle. *Nat Commun* 2024;15:8010.
Google Scholar Crossref PubMed WorldCat

50. Wieder WR. et al. Explicitly representing soil microbial processes in earth system models. *Glob Biogeochem Cycles* 2015;29:1782–800.
Google Scholar Crossref WorldCat